Water/Alcohol Soluble Thickness-Insensitive Hyperbranched Perylene Diimide Electron Transport Layer Improving the Efficiency of Organic Solar Cells

Dan Zhou [1,*] **, Fei Yang** [1] **, Yuancheng Qin** [1] **, Rong Zhong** [1] **, Haitao Xu** [2] **, Yongfen Tong** [1] **, Yubao Zhang** [3] **, Qin Zhang** [3] **, Mingjun Li** [1] **and Yu Xie** [1,*]

[1] Key Laboratory of Jiangxi Province for Persistent Pollutants, Control and Resources Recycle, Nanchang Hangkong University, 696 Fenghe South Avenue, Nanchang 330063, China; 15770938986@163.com (F.Y.); qinyuancheng@hotmail.com (Y.Q.); zhongr@nchu.edu.cn (R.Z.); 40019@nchu.edu.cn (Y.T.); limingjun@nchu.edu.cn (M.L.)

[2] College of Materials Science and Engineering, Nanchang Hangkong University, 696 Fenghe Avenue, Nanchang 330063, China; haitaoxu@nchu.edu.cn

[3] School of Measuring and Optical Engineering, Nanchang Hangkong University, Nanchang 330063, China; 70637@nchu.edu.cn (Y.Z.); 70433@nchu.edu.cn (Q.Z.)

* Correspondence: zhoudan@nchu.edu.cn (D.Z.); xieyu_121@163.com (Y.X.)

check for updates

Abstract: The electron transport layer (ETL) is very crucial for enhancing the device performance of polymer solar cells (PSCs). Meanwhile, thickness-insensitive and environment-friendly water/alcohol soluble processing are two essential requirements for large-scale roll-to-roll commercial application. Based on this, we designed and synthesized two new n-type ETLs with tetraethylene pentamine or butyl sulfonate sodium substituted tetraethylene pentamine as the branched side chains and high electron affinities perylene diimide (PDI) as the central core, named as **PDIPN** and **PDIPNSO₃Na**. Encouragingly, both **PDIPN** and **PDIPNSO₃Na** can effectively reduce the interfacial barrier and improve the interfacial contact. In addition, both of them can exhibit strong n-type self-doping effects, especially the **PDIPN** with higher density of negative charge. Consequently, compared to bare ITO, the PCE of the devices with ITO/**PDIPN** and ITO/**PDIPNSO₃Na** ETLs has increased to 3–4 times. Our research results indicate that n-type self-doping PDI-based ETL **PDIPN** and **PDIPNSO₃Na** could be promising candidates for ETL in environment-friendly water/alcohol soluble processing large-scale PSCs.

Keywords: thickness-insensitive; electron transport layer; perylene diimides

1. Introduction

Polymer solar cells (PSCs) have attracted increasing attention due to their lightweight, flexibility, and easy large-area solution processability [1–11]. With the rapid progress in novel donor and acceptor material design and interfacial engineering, the power conversion efficiency (PCE) of the PSCs have been boosted over 14% [12,13]. Currently, most research focuses on the design of novel active layer materials for improving the power conversion efficiency (PCE) of the PSCs [14–19]. Interfacial modulating is also very crucial for enhancing the PCE of the device [20–24].

The mismatched energy lever between the active layer and electrode can cause the Schottky barrier, thus inhibiting the charge transfer and injection [25]. Suitable interfacial modification can decrease the interfacial barrier and increase the selectivity of charge, thus inhibiting the charge recombination and increasing the efficiency of charge injection [26,27]. Hence, inserting an interlayer between active layer and cathode electrode should be an effective strategy to increase the performance of the device.

To date, metal oxide semiconductor (TiOx, ZnO, MoOx), electrolytes and fullerenes derivates etc have been used as ETLs to modulate interfacial contact and reduce interfacial barriers [28–34]. However, inorganic metal oxide ETL usually shows incompatible with the organic light harvest. Moreover, most of inorganic metal oxide ETLs need to be treated with a high temperature, which cannot be satisfied with the demand of the solution-process large-scale commercial application.

In consequence, to explore environment-friendly water/alcohol soluble processing organic ETL with strong interfacial control capability is extremely urgent. It would be better if the ETL is thickness-insensitive and can be efficient in different interlayer thickness. Perylene diimide (PDI) is a famous n-type material, which has many strong points, such as good electron affinities, high conductivities and facile modification by simple substitution reaction [35–38]. Moreover, the high conductivity of the PDI originated from self-organized p-stacks in solid film can endow the PDT-based ETL with thickness-insensitive superiority, which can conquer the thickness restriction (<10 nm) of the reported organic ETL. Thus, PDT-based ETL may have the potential to realize large-area manufacturing techniques owing to its tolerance of certain thickness variation.

N-type self-doping phenomena of the ETLs can enhance the electron mobility and form additional big interfacial dipoles on the interface of ITO and active layer [39]. Combining the PDI and n-type self-doping at molecular level can endow the material with the advantages of both materials. Tetraethylene pentamine contains enough polar groups and unpaired electrons of the N atoms. Inspired by this, we designed and synthesized two new n-type ETLs **PDIPN** and **PDIPNSO₃Na** (Scheme 1) with perylene diimide (PDI) as central core and tetraethylene pentamine or butyl sulfonate sodium substituted tetraethylene pentamine as the branched side chains. Intriguingly, both n-type ETLs **PDIPN** and **PDIPNSO₃Na** can form favorable interfacial dipole due to the polar groups and n-type self-doping effect. In sharp comparison to the device without ETL, the PCEs of the inverted device based on ITO/**PDIPN** and ITO/**PDIPNSO₃Na** have been increased over two times. Furthermore, both **PDIPN** and **PDIPNSO₃Na** can obtain an acceptable efficiency among a wide range of ETL thickness. As a result, environment-friendly water/alcohol soluble thickness-insensitive **PDIPN** and **PDIPNSO₃Na** should be a promising ETL for large-scale commercial application.
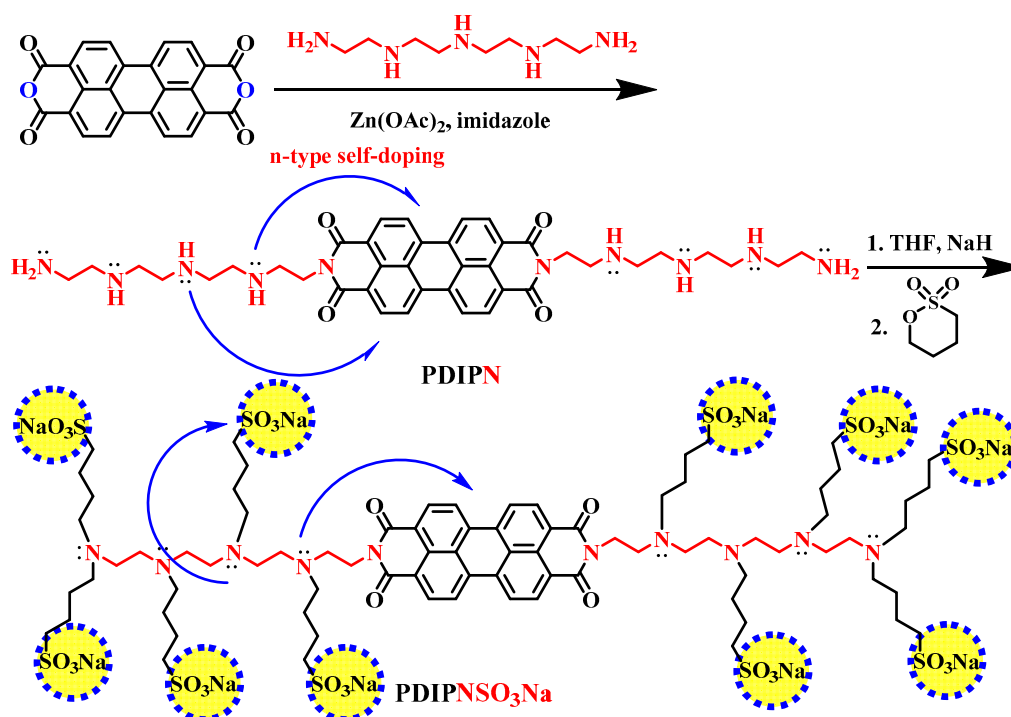
Scheme 1. Synthetic routes of **PDIPN** and **PDIPNSO₃Na**.

2. Synthesis and Characterization

The detailed synthetic procedures of the hyperbranched perylene diimides ETLs **PDIPN** and **PDIPNSO₃Na** are provided in Scheme 1, and the synthetic route is depicted in the Supporting Information. The **PDIPN** is synthesized by one-step substitution reaction between 3,4,9,10-perylenetetracarboxylic diimides and tetraethylene pentamine with a catalytic amount of zinc acetate (127 mg). The **PDIPNSO₃Na** is prepared by **PDIPN** with NaH and 1,4-butanesultone via simple substitution reaction. Due to the existence of the polar group, the **PDIPN** and **PDIPNSO₃Na** ETL can realize non-polluted water/alcohol processing. The structures of **PDIPN** and **PDIPNSO₃Na** are verified by ^{1}H nuclear magnetic resonance spectra (^{1}H NMR) (Figure S1–S2) and UV–Vis absorption (Figure 1).
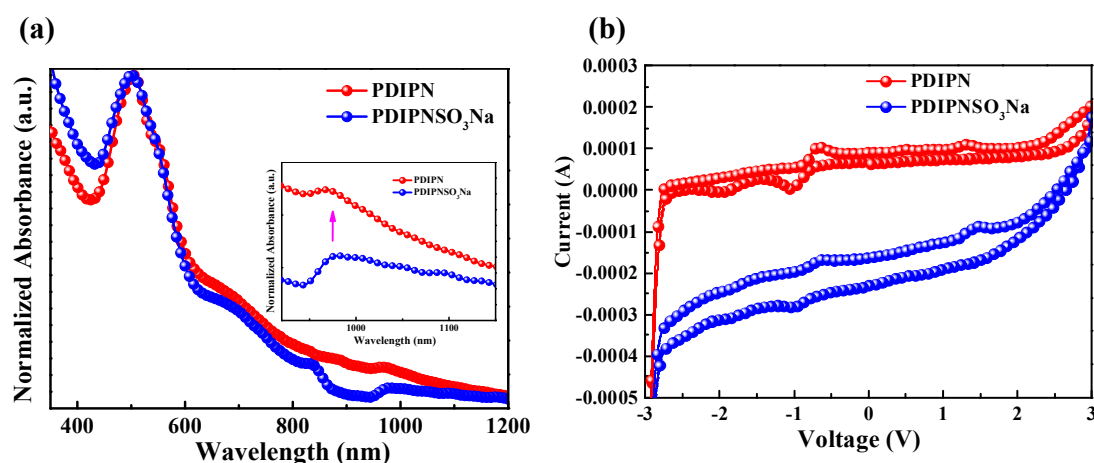

Figure 1. (**a**) UV–Vis absorption and (**b**) cyclic voltammograms (CV) spectra of **PDIPN** and **PDIPNSO₃Na** films.

To calculate the optical bandgap (E_g^{opt}) and electrochemical bandgap (E_g^{ec}) of the ETLs **PDIPN** and **PDIPNSO₃Na**, the UV−Vis and cyclic voltammetry (CV) are investigated, as shown in Figure 1. From Figure 1a, we can obviously see that the absorption band onset (λ_{onset}) of **PDIPN** and **PDIPNSO₃Na** are at 614 nm and 620 nm, an optical bandgap (E_g^{opt}) can be calculated to be 2.02 eV for **PDIPN** and 2.00 eV for **PDIPNSO₃Na**. Meanwhile, a broad absorption peak can be easily observed at 800 nm and extended to 1100 nm both in **PDIPN** and **PDIPNSO₃Na** film, which should be ascribed to the absorption of polarons [40–42]. These results suggest that maybe there are n-type self-doping effects exist in **PDIPN** and **PDIPNSO₃Na** owing to the existence of unpaired electron in N atoms [43]. The unpaired electron of the N atoms can transfer to the perylene diimidess nucleus, thus giving rise to the formation of n-type self-doping behavior. Furthermore, compared to **PDIPNSO₃Na**, **PDIPN** film shows stronger absorption band of polarons, indicating that the number of free electron of **PDIPN** is much more than that of **PDIPNSO₃Na**. Because one mole **PDIPNSO₃Na** has ten moles electron-withdrawing sodium sulfonate, the density of free electrons of **PDIPNSO₃Na** is lower than that of **PDIPN**. The n-type self-doping can form additional interfacial dipole, which is beneficial to reduce the interface barrier and enhance the electron injection efficiency, thus increasing the PCE of the device. The electrochemical energy levels are measured by cyclic voltammetry in an anhydrous nitrogen-saturated acetonitrile solution of n-Bu₄NPF₆, as depicted in Figure 1b. The **PDIPN** and **PDIPNSO₃Na** exhibit onset oxidation potentials at −0.73 eV and −0.79 eV, the HOMO of **PDIPN** and **PDIPNSO₃Na** are estimated to be −5.59 eV and −5.67 eV, respectively [44,45]. Meanwhile, we can calculate the LUMO of **PDIPN** and **PDIPNSO₃Na** to be −3.67 eV and −3.61 eV according to their onset reduction potentials; the detailed CV data are provided in Table S1.

To obtain further insight into the n-type self-doping behavior of **PDIPN** and **PDIPNSO₃Na**, the electron paramagnetic resonance (EPR) spectra are characterized. In Figure 2, obvious narrow

line shape signals at about 330G can be detected both in **PDIPN** and **PDIPNSO₃Na** films, these signals are consistent with the presence of unpaired electrons [43]. Moreover, in comparison to the **PDIPNSO₃Na**, the EPR signal of **PDIPN** is immensely stronger. These phenomena should because the density of negative charge of **PDIPNSO₃Na** has been significantly reduced owing to the electron-withdrawing sulfonate of the branched chain, hence inhibiting the electron from transferring to the perylene diimidess nucleus [42]. The result of the EPR is quite in agreement with that of the UV–Vis measurement. Furthermore, we can easily draw a conclusion that both **PDIPN** and **PDIPNSO₃Na** films possess n-type self-doping effect, and the **PDIPN** film show stronger n-type self-doping compared to that of **PDIPNSO₃Na**. The schematic diagram of self-doping process is shown in Scheme 1.
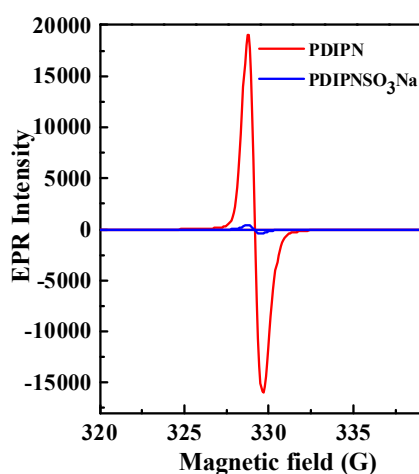

Figure 2. Electron paramagnetic resonance (EPR) spectra of the **PDIPN** and **PDIPNSO₃Na** film.

The X-ray photoelectron spectra (XPS) of pristine ITO and ITO/ETLs are conducted to investigate the interfacial interaction, as displayed in Figure 3a. Figure 3b is the N 1s XPS graph of the ITO, ITO/**PDIPN** and ITO/**PDIPNSO₃Na**. Obviously, there is no signal peak detected for bare ITO. Simultaneously, a broad peak at 400.04 eV is detected for ITO/**PDIPN**, which is associated to the N atoms of the imide and amine in **PDIPN**. Besides, for ITO/**PDIPNSO₃Na**, a broad strong peak at a value of 399.9 eV and a broad weak peak at 403.05 eV are found. Similarly, the peak at 399.9 eV belongs to the imide and amine. However, the new weak peak of 403.05 eV is assigned to $N(CH_2)_3H^+$. $N(CH_2)_3$ of **PDIPNSO₃Na** can be partially protonated and form $N(CH_2)_3H^+$ by reacting with the protons (H^+) from the water/methanol due to its basicity. From Figure 3c, a strong peak at 1070.80 eV is observed for ITO/**PDIPNSO₃Na**, which belongs to the sodium sulfonate branched chain. Nevertheless, Na 1s signal peaks cannot be traced in the spectra of ITO and ITO/**PDIPN** due to no Na element. The spectra of S 2p with different ETLs are shown in Figure 3d, there are no peaks in bare ITO and ITO/**PDIPN**, while an obvious peak at 168.04 eV has been found for ITO/**PDIPNSO₃Na** film, which should be ascribed to the absorption of S atom in -SO₃Na terminal groups. It indicates that **PDIPN** and **PDIPNSO₃Na** have been triumphantly synthesized and spin-coated on ITO according to the high-resolution N 1s, Na 1s and S 2p spectra.

The XPS spectra of the In 3d and Sn 3d are carried out to further characterize the interfacial interactions and interfacial dipole between **PDIPN** and **PDIPNSO₃Na** and ITO (Figure 4). In comparison to the In 3d of bare ITO (Figure 4a), the resolution peaks of both ITO/**PDIPN** and ITO/**PDIPNSO₃Na** have moved to lower binding energy. The shift of the In 3d signal indicates that strong interfacial interaction occurs at the interface of the ITO/**PDIPN** and ITO/**PDIPNSO₃Na**. Similarly, the Sn 3d XPS spectra of ITO, ITO/**PDIPN** and ITO/**PDIPNSO₃Na** are also studied (Figure 4b). Bare ITO exhibits the Sn 3d peaks at 494.50 eV and 486.15 eV, and the corresponding peaks of ITO/**PDIPN** shift toward lower binding energies to 494.35 eV and 486.10 eV, respectively, and the corresponding peaks of ITO/**PDIPNSO₃Na** are observed at 494.25 eV and 485.94 eV. Both the

In 3d and Sn 3d signals shift to lower binding energy could once again demonstrate that the interfacial dipoles are indeed created and strong interfacial interactions are in the presence of ITO/**PDIPN** and ITO/**PDIPNSO₃Na** interfaces. Interestingly, a strong broad peak at 497.00 eV has been detected for ITO/**PDIPNSO₃Na**, which owing to the Na (KLL) Auger peak. The existence of Na (KLL) Auger peak originates from the KLL energy level transition of Na atoms proves that the **PDIPNSO₃Na** film has been spin-coated on the ITO surface.
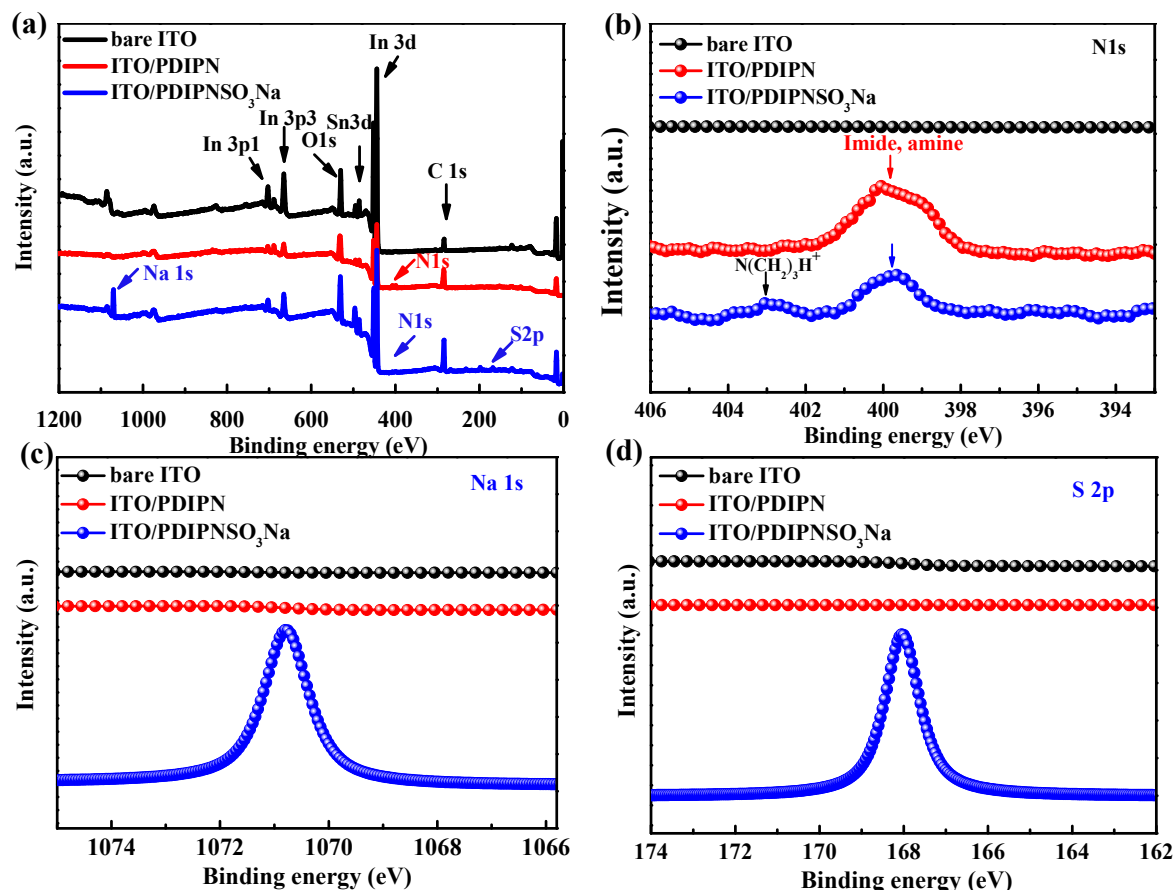

Figure 3. (**a**) Survey X-ray photoelectron spectra of bare ITO, ITO/**PDIPN** and ITO/**PDIPNSO₃Na** (**b**) N 1s, (**c**) Na 1s, (**d**) S 2p.
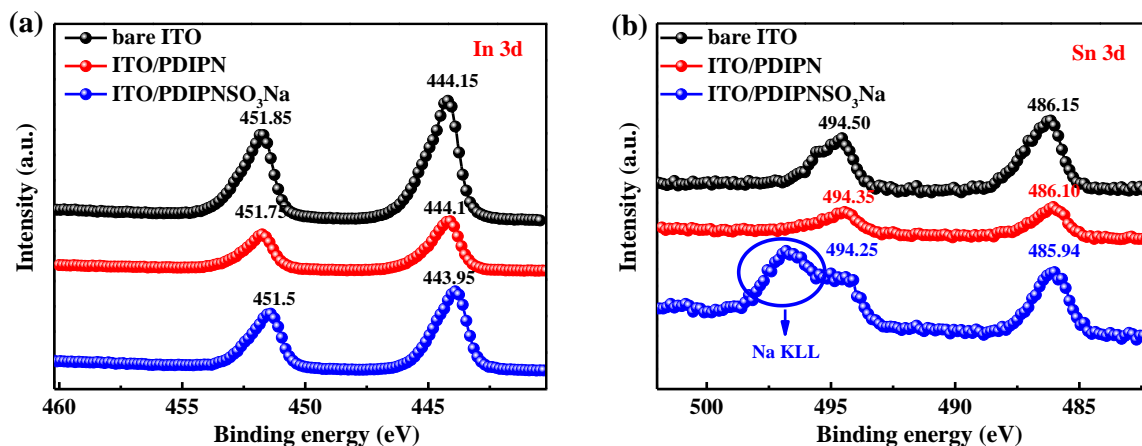

Figure 4. Survey X-ray photoelectron spectra of bare ITO, ITO/**PDIPN** and ITO/**PDIPNSO₃Na** (**a**) In 3d and (**b**) Sn 3d.

The polar branched chains of the **PDIPN** and **PDIPNSO$_3$Na** are inclined to create preferable dipoles at the interface of the metal cathode electrode and active layer, which give rise to the shift of the vacuum-level, thus modifying the work function (WF) of the electrode [46]. The ultraviolet photoelectron spectroscopy (UPS) is carried out to confirm the positive influence of the ETLs **PDIPN** and **PDIPNSO$_3$Na** on the WF of ITO (Figure 5a). The high binding energy cutoffs (E$_{cutoff}$) for reference ITO is 16.7 eV. However, the E$_{cutoff}$ of ITO has been shifted toward higher energy to 17.1 eV and 17.4 eV after modified by **PDIPN** and **PDIPNSO$_3$Na**, respectively. Simultaneously, there was a slight shift of E$_{onset}$. The E$_{onset}$ values of ITO, ITO/**PDIPN** and ITO/**PDIPNSO$_3$Na** are 0.10 eV, 0.05 eV and 0.19 eV. Based on the equation [47].: $-$HOMO = hν $-$ (E$_{cutoff}$ $-$ E$_{onset}$), hν = 21.22 eV, the HOMO values of ITO, ITO/**PDIPN** and ITO/**PDIPNSO$_3$Na** are -4.62 eV, -4.17 eV and -4.01 eV, respectively. Therefore, the WF differences (ΔΦ) among ITO, ITO/**PDIPN** and ITO/**PDIPNSO$_3$Na** are -0.45 eV and -0.61 eV. The shifts of the energy levels demonstrate that both the **PDIPN** and the **PDIPNSO$_3$Na** can indeed significantly lower the WF of ITO. The decreased WF of ITO originates from the interfacial dipole, manifesting that the interfacial dipole is 0.45 eV for ITO/**PDIPN** and 0.61 eV for ITO/**PDIPNSO$_3$Na**. The detailed energy levels data are provided in Table 1. Kelvin probe microscopy (KPM) is used to obtain more information about the impact of the interface dipoles on the WF of ITO, as shown in Figure 5b. Based on the KPM matrix spectra, we can distinctly discover that the WF of ITO has been reduced after modified by **PDIPN** and **PDIPNSO$_3$Na**. The bare ITO shows a WF of 4.70 eV. Intriguingly, compared to bare ITO, the WF values of ITO/**PDIPN** and ITO/**PDIPNSO$_3$Na** have been decreased by 0.50 eV and 0.54 eV. The KPM results are quite coincide to those of UPS. Moreover, on the basis of the results of UPS and KPM, we can once again verify the interfacial dipole in the interface between ITO/**PDIPN** and ITO/**PDIPNSO$_3$Na**. The interfacial dipole is beneficial to reduce the work function of ITO, thus reducing the electron injection barrier and enhancing the efficiencies of charge separation and transfer.
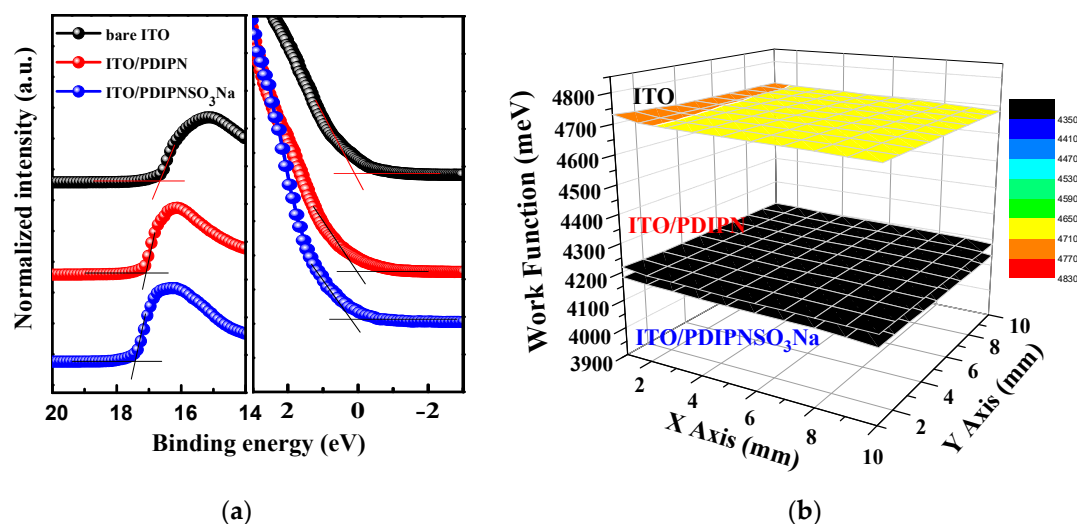

(**a**)   (**b**)

Figure 5. (**a**) Ultraviolet photoelectron spectroscopy (UPS) spectra of the inelastic cutoff region (left) and the HOMO region (right) of bare ITO, ITO/**PDIPN** and ITO/**PDIPNSO$_3$Na** ETLs and (**b**) Work function images from Kelvin probe microscopy matrix.

Table 1. Energy levels of the ITO, ITO/**PDIPN** and ITO/**PDIPNSO$_3$Na**.

ETL	E$_{cutoff}$ (eV)	E$_{oneset}$ (eV)	HOMO (eV)	[a] ΔΦ (eV)	KPM (eV)
ITO	16.7	0.10	-4.62	-	4.70
ITO/**PDIPN**	17.1	0.05	-4.17	-0.45	4.20
ITO/**PDIPNSO$_3$Na**	17.4	0.19	-4.01	-0.61	4.16

[a] ΔΦ means the difference in the work function of ITO, ITO/**PDIPN** and ITO/**PDIPNSO$_3$Na** according to the UPS, $-$HOMO = hν $-$ (E$_{cutoff}$ $-$ E$_{onset}$), hν = 21.22 eV.

Surface morphology of the electron transport layer is very important for the charge separation and transfer. The atomic force microscopy (AFM) is measured to characterize the surface morphology of ITO/**PDIPN** and ITO/**PDIPNSO₃Na**. Figure S3a,b are the height images of ITO/**PDIPN** and ITO/**PDIPNSO₃Na**, and Figure S3c,d are the corresponding phase images. Delightfully, both **PDIPN** and **PDIPNSO₃Na** can form homogeneous morphology on the surface of ITO. The root-mean-square (RMS) roughness of ITO/**PDIPN** is 3.36 nm, and the RMS ITO/**PDIPNSO₃Na** 3.22 nm. Besides, the three-dimensional AFM image of ITO, ITO/**PDIPN** and ITO/**PDIPNSO₃Na** are presented in Figure S4. The homogeneous and smooth morphology of ETL can facilitate charge transfer and transportation. In addition, the AFM images of the active layer are measured to confirm that whether the surface can become smoother by inserting **PDIPN** and **PDIPNSO₃Na** than that of without the presence of any ETL (Figure 6). In comparison to ITO/P3HT:PC$_{61}$BM with a RMS roughness of 11.3 nm, the RMS roughness of ITO/**PDIPN**/P3HT:PC$_{61}$BM and ITO/**PDIPNSO₃Na**/P3HT:PC$_{61}$BM is decreased to 6.55 nm and 9.45 nm, manifesting that both **PDIPN** and **PDIPNSO₃Na** ETL can exert a positive influence on the morphology of the corresponding active layer. The smoother morphology of the active layer is in favor of charge separation and transfer.
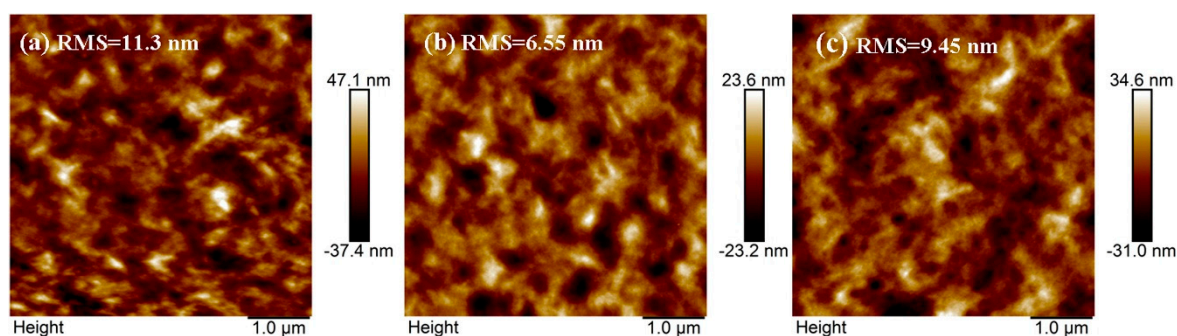

Figure 6. Atomic force microscopy (AFM) tapping mode height images the surface of (**a**) ITO/P3HT:PC$_{61}$BM, (**b**) ITO/**PDIPN**/P3HT:PC$_{61}$BM and (**c**) ITO/**PDIPNSO₃Na**/P3HT:PC$_{61}$BM.

To verify the positive roles of **PDIPN** and **PDIPNSO₃Na** ETLs in the PSCs, the **PDIPN** and **PDIPNSO₃Na** ETLs corresponding to inverted devices are fabricated. The schematic representation of the inverted device structure and an energy levels diagram of the PSCs are shown in Figure 7. From the energy levels diagram, we can clearly observe that both the LUMO levels of ITO/**PDIPN** and ITO/**PDIPNSO₃Na** are higher than that of PC$_{61}$BM, indicating that ohmic contact can be formed after inserting **PDIPN and PDIPNSO₃Na** ETLs. Meanwhile, compared to the HOMO level of P3HT, the ITO/**PDIPN** and ITO/**PDIPNSO₃Na** have lower HOMO levels, revealing that both **PDIPN and PDIPNSO₃Na** ETLs can block the hole transport.
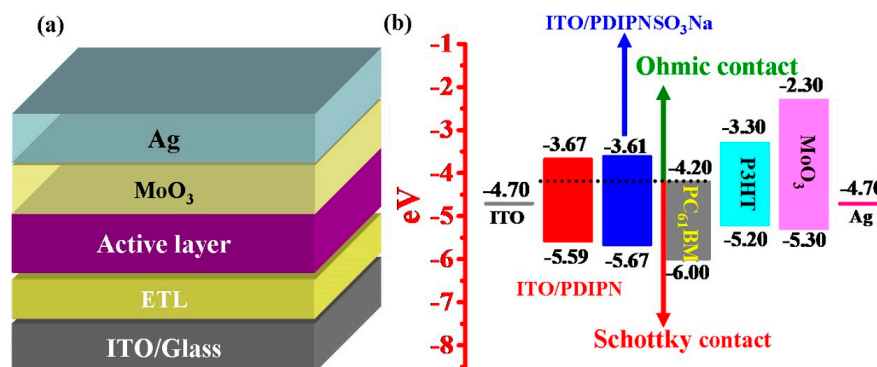

Figure 7. (**a**) The inverted device structure of the PSC. (**b**) Energy-level diagram of the PSCs.

The *J-V* spectra of the device based on ITO, ITO/**PDIPN** and ITO/**PDIPNSO₃Na** are described in Figure 8a, and the relevant device performance data with different ETLs and different thicknesses

are filled in Table S2. The $J-V$ characteristics of the devices of ITO/**PDIPN** and ITO/**PDIPNSO₃Na** with different thicknesses are supplemented in Figure S5. The device with ITO obtains a PCE of 0.9%. Delightfully, after modified by **PDIPN** (11 nm), the PCE has been dramatically increased to 3.5% with a V_{oc} of 0.61 V, a J_{sc} of 8.95 mA/cm^2 and a fill factor (FF) of 64.8%. Meanwhile, the device with ITO/**PDIPNSO₃Na** (11 nm) shows a PCE of 3.1%, which is significantly improved compared to that of ITO. It is noteworthy that all the device parameters based on ITO/**PDIPN** and ITO/**PDIPNSO₃Na**, including V_{oc}, J_{sc}, PCE, and FF parameters have been significantly enhanced compared to that of bare ITO. The enhanced device properties should due to the improved interfacial contact and n-type self-doping effect. Manifestly, the photovoltaic performance of ITO/**PDIPN** is slightly higher than that of ITO/**PDIPNSO₃Na** under the same condition, the higher PCE originates from the higher J_{sc} and FF. Compared to ITO/**PDIPNSO₃Na**, the better performance of ITO/**PDIPN** could owing to its stronger n-type self-doping effect. As we known, the higher n-type self-doping effect is favorable for charge transfer, thus enhancing the J_{sc} and FF of the corresponding device. Moreover, when the thicknesses of the ITO/**PDIPN** and ITO/**PDIPNSO₃Na** are increased to 28 nm, the devices can still achieve an acceptable PCE of 3.1% and 2.8%, respectively. The n-type essence of **PDIPN** and **PDIPNSO₃Na** can endow them with thickness-insensitive superiority. The thickness-insensitive advantages can make them more suitable for large-scale commercial printing production. To further discuss the effects of the **PDIPN** and **PDIPNSO₃Na** on the photovoltaic properties, the dark $J-V$ curves are studied in the inset of Figure 8a. Encouragingly, the dark current densities of ITO/**PDIPN** and ITO/**PDIPNSO₃Na** ETLs are dramatically smaller than that of bare ITO under the reverse bias, suggesting that the charge recombination has been significantly inhibited by the contribution of **PDIPN** and **PDIPNSO₃Na** ETLs. The dark $J-V$ curves can further manifest that the preferable interfacial dipoles originate from the polar branched chain and n-type self-doping effect of **PDIPN** and **PDIPNSO₃Na** can efficiently suppress the leakage current, therefore increasing the charge injection efficiency of the devices. The research results of the dark $J-V$ curves are in accordance with that of illuminated $J-V$.
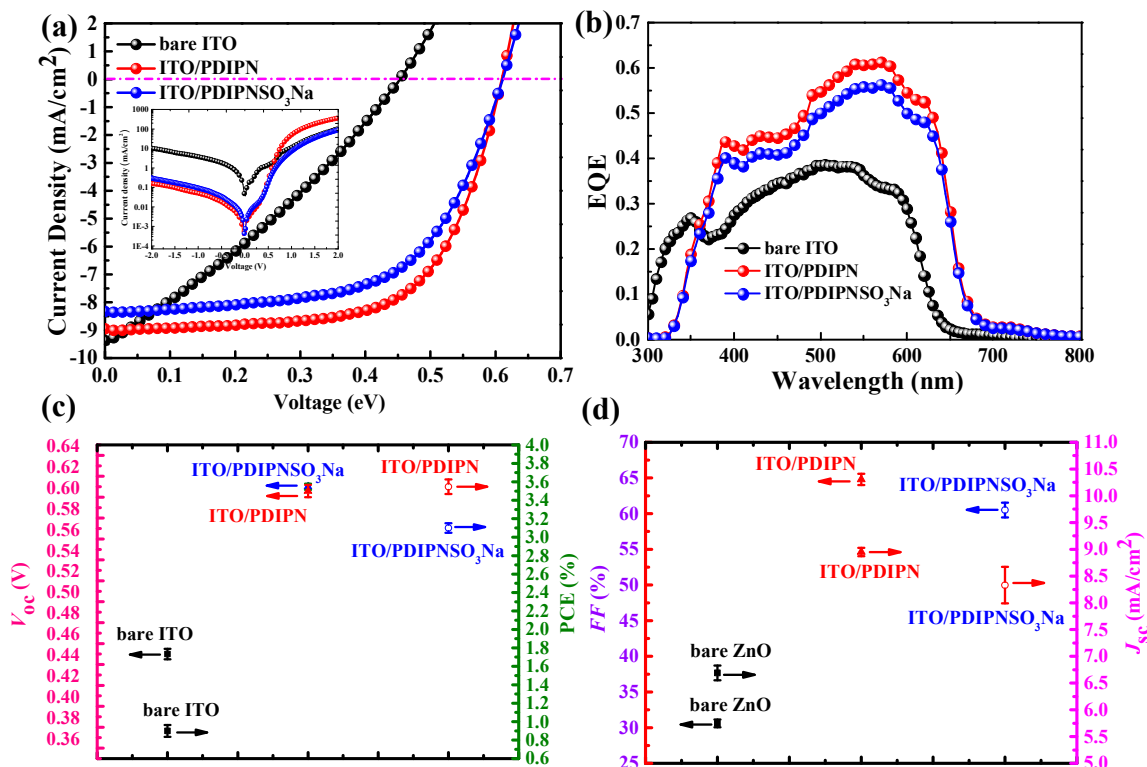

Figure 8. (**a**) $J-V$ curves of devices based on P3HT:PC$_{61}$BM with various ETLs under the illumination of AM1.5G, 100 mW cm^{-2} (inset: under dark conditions), (**b**) EQE characteristics, (**c**) The standard deviations error bars of V_{oc} and PCE and (**d**) the standard deviations error bars of and FF and J_{sc}.

The external quantum efficiency (EQE) has been measured to make further consideration of the interfacial dipoles on the J_{sc}, as presented in Figure 8b. From the skeleton diagram of the EQE, we can clearly see that both ITO/**PDIPN** and ITO/**PDIPNSO$_3$Na** show more outstanding external quantum efficiency between 350 and 700 nm than bare ITO. Notably, ITO/**PDIPN** ETL exhibits the highest value among the three devices. The results from EQE are quite in consistent with those acquired from illuminated and dark $J-V$ characteristic. In brief, due to their interfacial modulating and thickness-insensitive properties, both **PDIPN** and **PDIPNSO$_3$Na** may become potential candidates as ETLs in polymer solar cells, especially for large-scale solution-processed PSCs. The integrated current values from EQE for ITO/**PDIPN** and ITO/**PDIPNSO$_3$Na** are 8.90 mA/cm^2 and 8.19 mA/cm^2. The standard deviations error bars of V_{oc}, PCE, *FF* and J_{sc} are shown in Figure 8c,d, and the detailed information are shown in Table 2.

Table 2. Device Performance of the Inverted P3HT:PC$_{61}$BM Polymer Solar Cells with Various ETLs.

Cathode Buffer Layer	V_{oc} (V)	J_{sc} (mA/cm^2)	*FF* (%)	PCE (%)
ITO	0.45 ± 0.005	6.69 ± 0.138	30.6 ± 0.54	0.9 ± 0.064
ITO/**PDIPN** (11 nm)	0.61 ± 0.003	8.95 ± 0.078	64.8 ± 0.79	3.5 ± 0.067
ITO/**PDIPNSO$_3$Na** (11 nm)	0.61 ± 0.007	8.33 ± 0.341	60.5 ± 1.03	3.1 ± 0.052

The device parameters of each device are obtained from 10 devices, and the ± refer to the standard deviation.

The $J-V$ characteristics of electron-only devices based on P3HT:PC$_{61}$BM blends are measured to get more information regarding electronic mobility, as displayed in Figure 9. The bare-ITO device shows a low electronic mobility of 9.45×10^{-7} cm^2 V^{-1} s^{-1}. However, when inserting **PDIPNSO$_3$Na** as ETL, the electronic mobility has been dramatically increased to 1.61×10^{-4} cm^2 V^{-1} s^{-1}. Moreover, in contrast to ITO/**PDIPNSO$_3$Na**, the device with ITO/**PDIPN** ETL exhibits better electronic mobility of 4.18×10^{-4} cm^2 V^{-1} s^{-1}, which should be ascribed to the latter possesses higher n-type self-doping effect, thus supporting higher electronic mobility and higher J_{sc}. These results agree well with the electron paramagnetic resonance and $J-V$ spectra.
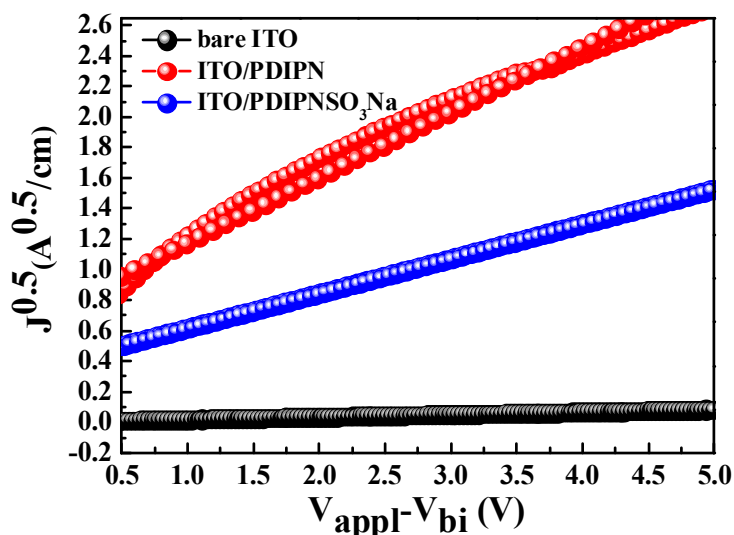

Figure 9. $J^{0.5}-V$ characteristics of electron-only devices ITO/ETLs/P3HT:PC$_{61}$BM/Al with bare ITO, ITO/**PDIPN** and ITO/**PDIPNSO$_3$Na** ETLs.

3. Conclusions

In conclusion, two new n-type water/alcohol-soluble thickness-insensitive ETLs **PDIPN** and **PDIPNSO$_3$Na** have been first designed and synthesized as ETL in PSCs. The appropriate energy levels and WF tuning properties of **PDIPN** and **PDIPNSO$_3$Na** cause the corresponding PSCs to

have acceptable PCE on a relatively broad range of interlayer thickness, especially in the device based on **PDIPN** ETL. Compared to the counterpart **PDIPNSO₃Na**, **PDIPN** with higher density of an unpaired electron exhibits higher n-type self-doping effect, thus, contributing to higher J_{sc}, FF and PCE. In comparison to ITO-only devices, the PCE of the device based on ITO/**PDIPN** and ITO/**PDIPNSO₃Na** ETLs has been increased from 0.9% to 3.1% and 3.5%, respectively. The outstanding properties of **PDIPN** and **PDIPNSO₃Na** should make them potential candidates as ETL in solution-processed high-efficiency organic photovoltaic devices.

Supplementary Materials: Supplementary materials can be found at http://www.mdpi.com/2073-4360/11/4/655/s1.

Author Contributions: Data curation, F.Y. and Q.Z.; Methodology, Y.Q.; Project administration, D.Z.; Resources, H.X., Y.T. and Y.Z.; Supervision, M.L. and Y.X.; Validation, R.Z.

Conflicts of Interest: The authors declare they have no conflict of interest.

References

1. Oh, S.H.; Na, S.I.; Jo, J.; Lim, B.; Vak, D.; Kim, D.Y. Water-Soluble Polyfluorenes as an Interfacial Layer Leading to Cathode-Independent High Performance of Organic Solar Cells. *Adv. Funct. Mater.* **2010**, *20*, 1977–1983. [CrossRef]

2. Zhou, D.; Xiong, S.; Chen, L.; Cheng, X.; Xu, H.; Zhou, Y.; Liu, F.; Chen, Y. A green route to a novel hyperbranched electrolyte interlayer for nonfullerene polymer solar cells with over 11% efficiency. *Chem. Commun.* **2018**, *54*, 563–566. [CrossRef]

3. Ouyang, X.; Peng, R.; Ai, L.; Zhang, X.; Ge, Z. Efficient polymer solar cells employing a non-conjugated small-molecule electrolyte. *Nature Photon.* **2015**, *9*, 520. [CrossRef]

4. Qin, Y.; Liu, S.; Gu, H.; Dai, W.; Luo, X. Highly flattened donor-acceptor polymers based on fluoride-substituent acceptors for efficient heterojunction solar cells. *Sol. Energy* **2018**, *166*, 450–457. [CrossRef]

5. Zhang, X.; Zhang, B.; Ouyang, X.; Chen, L.; Wu, H. Polymer solar cells employing water-soluble polypyrrole nanoparticles as dopants of PEDOT: PSS with enhanced efficiency and stability. *J. Phys. Chem. C* **2017**, *121*, 18378–18384. [CrossRef]

6. Jiang, W.; Yu, R.; Liu, Z.; Peng, R.; Mi, D.; Hong, L.; Wei, Q.; Hou, J.; Kuang, Y.; Ge, Z. Ternary nonfullerene polymer solar cells with 12.16% efficiency by introducing one acceptor with cascading energy level and complementary absorption. *Adv. Mater.* **2018**, *30*, 1703005. [CrossRef]

7. Jin, R.; Wang, F.; Guan, R.; Zheng, X.; Zhang, T. Design of perylene-diimides-based small-molecules semiconductors for organic solar cells. *Mol. Phys.* **2017**, *115*, 1591–1597. [CrossRef]

8. Liu, M.; Yang, J.; Yin, Y.; Zhang, Y.; Zhou, E.; Guoa, F.; Zhaoa, L. Novel perylene diimide-based polymers with electron-deficient segments as the comonomer for efficient all-polymer solar cells. *J. Mater. Chem. A* **2018**, *6*, 414–422. [CrossRef]

9. Gopalan, S.A.; Gopalan, A.I.; Vinu, A.; Lee, K.P.; Kang, S.W. A new optical-electrical integrated buffer layer design based on gold nanoparticles tethered thiol containing sulfonated polyaniline towards enhancement of solar cell performance. *Sol. Energy Mater. Sol. Cells* **2018**, *174*, 112–123. [CrossRef]

10. Xu, B.; Sai-Anand, G.; Jeong, H.M.; Kim, S.W.; Kim, J.S.; Kwon, J.B.; Kang, S.W. Improving Air-Stability and Performance of Bulk Heterojunction Polymer Solar Cells Using Solvent Engineered Hole Selective Interlayer. *Materials* **2018**, *11*, 1143. [CrossRef]

11. Sai-Anand, G.; Dubey, A.; Gopalan, A.I.; Venkatesan, S.; Ruban, S.; Rezac, K.M.; Choib, J.; Lakhi, K.S.; Xu, B.; Qiao, Q.; et al. Additive assisted morphological optimization of photoactive layer in polymer solar cells. *Sol. Energy Mater. Sol. Cells* **2018**, *182*, 246–254. [CrossRef]

12. Zhang, S.; Qin, Y.; Zhu, J.; Hou, J. Over 14% efficiency in polymer solar cells enabled by a chlorinated polymer donor. *Adv. Mater.* **2018**, *30*, 1800868. [CrossRef]

13. Cui, Y.; Yao, H.; Yang, C.; Zhang, S.; Hou, J. Organic solar cells with an efficiency approaching 15%. *Acta Polym. Sinica* **2018**, *2*, 223–230.

14. Sun, Y.; Fu, H.; Wang, Z. Polymer Donors for High-performance Non-fullerene Organic Solar Cells. *Angew. Chem. Int. Ed.* **2018**, *58*, 4442–4453.

15. Bi, P.; Hao, X. Versatile Ternary Approach for Novel Organic Solar Cells: A Review. *Sol. RRL* **2019**, *3*, 1800263. [CrossRef]

16. Li, S.; Ye, L.; Zhao, W.; Yan, H.; Yang, B.; Liu, D.; Li, W.; Ade, H.; Hou, J. A wide band gap polymer with a deep highest occupied molecular orbital level enables 14.2% efficiency in polymer solar cells. *J. Am. Chem. Soc.* **2018**, *140*, 7159–7167. [CrossRef]

17. Li, T.; Dai, S.; Ke, Z.; Yang, L.; Wang, J.; Yan, C.; Ma, W.; Zhan, X. Fused Tris (thienothiophene)-Based Electron Acceptor with Strong Near-Infrared Absorption for High-Performance As-Cast Solar Cells. *Adv. Mater.* **2018**, *30*, 1705969. [CrossRef]

18. Yao, Z.; Liao, X.; Gao, K.; Lin, F.; Xu, X.; Shi, X.; Zuo, L.; Liu, F.; Chen, Y.; Jen, A.Y. Dithienopicenocarbazole-based acceptors for efficient organic solar cells with optoelectronic response over 1000 nm and an extremely low energy loss. *J. Am. Chem. Soc.* **2018**, *140*, 2054–2057. [CrossRef]

19. Kan, B.; Feng, H.; Yao, H.; Chang, M.; Wan, X.; Li, C.; Hou, J.; Chen, Y. A chlorinated low-bandgap small-molecule acceptor for organic solar cells with 14.1% efficiency and low energy loss. *Sci. China Chem.* **2018**, *61*, 1307–1313. [CrossRef]

20. Po, R.; Carbonera, C.; Bernardi, A.; Camaioni, N. The role of buffer layers in polymer solar cells. *Energy Environ. Sci.* **2011**, *4*, 285–310. [CrossRef]

21. Sai-Anand, G.; Gopalan, A.I.; Lee, K.P.; Venkatesan, S.; Qiao, Q.; Kang, B.H.; Lee, S.W.; Lee, J.S.; Kang, S.W. Electrostatic nanoassembly of contact interfacial layer for enhanced photovoltaic performance in polymer solar cells. *Sol. Energy Mater. Sol. Cells* **2016**, *153*, 148–163. [CrossRef]

22. Sai-Anand, G.; Gopalan, A.I.; Lee, K.P.; Venkatesan, S.; Kang, B.H.; Lee, S.W.; Lee, J.S.; Qiao, Q.; Kwon, D.H.; Kang, S.W. A futuristic strategy to influence the solar cell performance using fixed and mobile dopants incorporated sulfonated polyaniline based buffer layer. *Sol. Energy Mater. Sol. Cells* **2015**, *141*, 275–290. [CrossRef]

23. Xu, B.; Sai-Anand, G.; Gopalan, A.I.; Muthuchamy, N.; Lee, K.P.; Lee, J.S.; Jiang, Y.; Lee, S.W.; Kim, S.W.; Kim, J.S.; et al. Functional solid additive modified PEDOT:PSS as an anode buffer layer for enhanced photovoltaic performance and stability in polymer solar cells. *Sci. Rep.* **2017**, *7*, 45079. [CrossRef]

24. Jiang, Y.; Sai-Anand, G.; Xu, B.; Lee, J.S.; Kim, S.W.; Yeom, S.H.; Bae, J.H.; Kang, S.W. Enhancing the photovoltaic performance of polymer solar cells by manipulating photoactive/metal interface. *J. Nanosci. Nanotechnol.* **2017**, *17*, 8024–8030. [CrossRef]

25. Hu, L.; Wu, F.; Li, C.; Hu, A.; Hu, X.; Zhang, Y.; Chen, L.; Chen, Y. Alcohol-soluble n-type conjugated polyelectrolyte as electron transport layer for polymer solar cells. *Macromolecules* **2015**, *48*, 5578–5586. [CrossRef]

26. Yang, B.; Zhang, S.; Li, S.; Yao, H.; Li, W.; Hou, J. A Self-Organized Poly (vinylpyrrolidone)-Based Cathode Interlayer in Inverted Fullerene-Free Organic Solar Cells. *Adv. Mater.* **2019**, 1804657. [CrossRef]

27. Liu, G.; Ji, S.; Xu, G.; Ye, C. Interface engineering: Boosting the energy conversion efficiencies for nanostructured solar cells. *Pure Appl. Chem.* **2012**, *84*, 2653–2675. [CrossRef]

28. Li, Y.; Zhao, Y.; Chen, Q.; Yang, Y.; Liu, Y.; Hong, Z.; Liu, Z.; Hsieh, Y.T.; Meng, L.; Li, Y.; et al. Multifunctional fullerene derivative for interface engineering in perovskite solar cells. *J. Am. Chem. Soc.* **2015**, *137*, 15540–15547. [CrossRef]

29. Zhou, D.; Xu, H.; Qin, Y.; Zhong, X.; Li, M.; Hu, B.; Tong, Y.; Xie, Y. Hyperbranched small-molecule electrolyte as cathode interfacial layers for improving the efficiency of organic photovoltaics. *J. Mater. Sci.* **2018**, *53*, 7715–7724. [CrossRef]

30. Qi, B.; Zhang, Z.G.; Wang, J. Uncovering the role of cathode buffer layer in organic solar cells. *Sci. Rep.* **2015**, *5*, 7803. [CrossRef]

31. Subbiah, J.; Mitchell, V.D.; Hui, N.K.C.; Jones, D.J.; Wong, W.W.H. A Green Route to Conjugated Polyelectrolyte Interlayers for High-Performance Solar Cells. *Angew. Chem. Int. Ed.* **2017**, *56*, 8431–8434. [CrossRef]

32. Wang, Z.; Zheng, N.; Zhang, W.; Yan, H.; Xie, Z.; Ma, Y.; Huang, F.; Cao, Y. Self-Doped, n-Type Perylene Diimide Derivatives as Electron Transporting Layers for High-Efficiency Polymer Solar Cells. *Adv. Energy Mater.* **2017**, *7*, 1700232. [CrossRef]

33. Nakano, K.; Tajima, K. Organic Planar Heterojunctions:From Models for Interfaces in Bulk Heterojunctions to High-Performance Solar Cells. *Adv. Mater.* **2017**, *29*, 1603269. [CrossRef]

34. Lee, B.R.; Lee, S.; Park, J.H.; Jung, E.D.; Yu, J.C.; Nam, Y.S.; Heo, J.; Kim, J.Y.; Kim, B.S.; Song, M.H. Amine-Based Interfacial Molecules for Inverted Polymer-Based Optoelectronic Devices. *Adv. Mater.* **2015**, *27*, 3553–3559. [CrossRef]

35. Yue, W.; Lv, A.; Gao, J.; Jiang, W.; Hao, L.; Li, C.; Li, Y.; Polander, L.E.; Barlow, S.; Hu, W.; et al. Hybrid rylene arrays via combination of stille coupling and C–H transformation as high-performance electron transport materials. *J. Am. Chem. Soc.* **2012**, *134*, 5770–5773. [CrossRef]

36. Mikroyannidis, J.A.; Stylianakis, M.M.; Suresh, P.; Roy, M.S.; Sharma, G.D. Synthesis of perylene monoimide derivative and its use for quasi-solid-state dye-sensitized solar cells based on bare and modified nano-crystalline ZnO photoelectrodes. *Energy Environ. Sci.* **2009**, *2*, 1293–1301. [CrossRef]

37. Huang, C.; Barlow, S.; Marder, S.R. Perylene-3, 4, 9, 10-tetracarboxylic acid diimides: Synthesis, physical properties, and use in organic electronics. *J. Org. Chem.* **2011**, *76*, 2386–2407. [CrossRef]

38. Dubey, R.K.; Westerveld, N.; Eustace, S.J.; Sudhölter, E.J.R.; Grozema, F.C.; Jager, W.F. Synthesis of Perylene-3,4,9,10-tetracarboxylic Acid Derivatives Bearing Four Different Substituents at the Perylene Core. *Org. Lett.* **2016**, *18*, 5648–5651. [CrossRef]

39. Chen, L.; Tan, Y.; Liu, X.; Chen, Y. Counterion induced facile self-doping and tunable interfacial dipoles of small molecular electrolytes for efficient polymer solar cells. *Nano Energy* **2016**, *27*, 492–498. [CrossRef]

40. Sun, Z.W.; Frank, A.J. Characterization of the intrachain charge-generation mechanism of electronically conductive poly (3-methylthiophene). *J. Chem. Phys.* **1991**, *94*, 4600–4608. [CrossRef]

41. Mai, C.K.; Zhou, H.; Zhang, Y.; Henson, Z.B.; Nguyen, T.Q.; Heeger, A.J.; Bazan, G.C. Facile Doping of Anionic Narrow-Band-Gap Conjugated Polyelectrolytes During Dialysis. *Angew. Chem. Int. Ed.* **2013**, *52*, 12874–12878. [CrossRef]

42. Russ, B.; Robb, M.J.; Popere, B.C.; Perry, E.E.; Mai, C.K.; Fronk, S.L.; Patel, S.N.; Mates, T.E.; Bazan, G.C.; Urban, J.J.; et al. Tethered tertiary amines as solid-state n-type dopants for solution-processable organic semiconductors. *Chem. Sci.* **2016**, *7*, 1914–1919. [CrossRef]

43. Patil, A.O.; Ikenoue, Y.; Basescu, N.; Colaneri, N.; Chen, J.; Wudl, F.; Heeger, A.J. Self-doped conducting polymers. *Synth. Met.* **1987**, *20*, 151–159. [CrossRef]

44. Bredas, J.L.; Silbey, R.; Boudreaux, D.S.; Chance, R.R. Chain-length dependence of electronic and electrochemical properties of conjugated systems: Polyacetylene, polyphenylene, polythiophene, and polypyrrole. *J. Am. Chem. Soc.* **1983**, *105*, 6555–6559. [CrossRef]

45. De Leeuw, D.M.; Simenon, M.M.J.; Brown, A.R.; Einerhand, R.E.F. Stability of n-type doped conducting polymers and consequences for polymeric microelectronic devices. *Synth. Met.* **1997**, *87*, 53–59. [CrossRef]

46. Kang, R.; Oh, S.H.; Kim, D.Y. Influence of the ionic functionalities of polyfluorene derivatives as a cathode interfacial layer on inverted polymer solar cells. *ACS Appl. Mater. Interfaces* **2014**, *6*, 6227–6236. [CrossRef]

47. Braun, S.; Salaneck, W.R.; Fahlman, M. Energy-level alignment at organic/metal and organic/organic interfaces. *Adv. Mater.* **2009**, *21*, 1450–1472. [CrossRef]